

IAC-20,A7,3,7,x57894

Wavelength Calibration of the Full-sun Ultraviolet Rocket SpecTrograph (FURST)

Nicolas Donders ^{a,b}, Amy Winebarger ^c, Charles Kankelborg ^d, Genevieve Vigil ^c, Laurel Rachmeler ^e, Ken Kobayashi ^c, Gary Zank ^{a,b}

^a *Department of Space Science, University of Alabama in Huntsville*

^b *Center for Space Plasma and Aeronomic Research, University of Alabama in Huntsville*

^c *Marshall Space Flight Center, NASA, Huntsville AL*

^d *Solar Group, Department of Physics, Montana State University, Bozeman MT*

^e *National Centers for Environmental Information, NOAA, Boulder CO*

Abstract

The Sun has a well-known periodicity in sunspot number and magnetic field variation. The underlying cause of this 11-year cycle is not fully understood and has yet to be connected with those processes in other stellar objects. The Full-sun Ultraviolet Rocket SpecTrograph (FURST) is a sounding rocket payload being developed by Montana State University (MSU) alongside the Marshall Space Flight Center (MSFC) solar physics group. Scheduled to launch from White Sands Missile Range (WSMR) in 2022, this instrument is unique in that it will provide the connection between stellar observatories with measurements of our Sun. It will achieve this through extremely high-resolution full-disk spectroscopy in EUV. We aim to obtain a wavelength resolution $R > 10,000$ in the 115 - 181 nm range, on par with that of the Hubble (HST) Space Telescope Imaging Spectrograph (STIS). The Lyman Alpha line (121 nm) is known to oversaturate most CCD electronics and is of particular challenge for this spectral range. In addition, this resolution goal will allow us to study the 3 km/s motion (a Doppler-shift of about 0.01 Angstroms) of the relatively low-temperature plasma in the chromosphere and lower corona.

This paper will present the results of our simulation of the diagnostic lamp signal to be used in this wavelength calibration. To test the viability of this precise of a device, we are building a collimator capable of calibrating the FURST instrument under these strict radiometric requirements. By way of a diagnostic lamp simulation, we will account for photon noise, CCD electronic readout noise, and statistical error. These will lead to the development of our pre- and post-launch calibration plan. Future work includes absolute radiometric and wavelength calibration with this new collimator. In addition, the ability of FURST to measure extremely small Doppler-shifts will provide capabilities for planetary atmospheric scientists. This impact is coupled with the diverse international partnership created by the closely-knit Sounding Rocket teams across the globe. These Sounding Rockets have an even broader impact, as they encourage future satellite missions under the prospect of long-term observations.

1 Introduction

The Sounding Rocket team at NASA's Marshall Space Flight Center (MSFC) have been producing unique optical experiments as part of the Solar Physics group [Tsuneta et al., 2008, Kano et al., 2012, Ishikawa et al., 2017]. While some current missions are set to look at X-rays (MaGIXS, Kobayashi et al. [2018]), and others will study active flaring regions (Hi-C Flare, see Kobayashi et al. [2014] and Winebarger et al. [2019]), the Full-sun Ultraviolet Rocket Spectrograph (FURST) is different [Kankelborg et al., 2017]. It is foremost a partnership between MSFC and Montana State University (MSU).

The focus for this payload is to produce a full-disk spectral image in the Vacuum UltraViolet (VUV) range, specifically between 1200 - 1810 Å. This wavelength region includes many important energy lines,

such as Lyman Alpha. Additionally, the resolution goals of FURST far outpace the data currently available. Such spectral lines have been well characterized in other stars by missions like the Hubble Space Telescope (HST). While FURST aims for an $R > 10,000$, HST only has an $R \approx 1,000$ for our Sun in this VUV range. [Woods et al., 2010].

In order to achieve this, the FURST instrument in particular has some unique optical characteristics. A typical spectrograph utilizes a slit aperture open to a grating mirror. The FURST instrument instead takes in a full-disk image and creates a "slit" by way of optical cylinders. Each cylinder is tuned and placed precisely around the Rowland circle such that they reflect towards a grating and then a CCD. To cover the desired 610 Å range with high precision, there are seven optical cylinders combined with a shutter system which reflect ≈ 104 Å at a time towards the

grating. When the experiments are performed, the signal received by a spectroscopic detector is translated from an electronic transmission at each pixel to an intensity of spectral lines.

Mapping every pixel to its corresponding wavelength requires calibration prior to the experiment. In practice, we will want to know the difference between the width and location of these Gaussian curves with respect to their expected / theoretical values. This will help to answer a key science goal, since the difference is caused by Doppler-shifts and thermal broadening due to solar activity. Thus, it becomes imperative to know the expected location so that we can functionally map each pixel number to a specific wavelength. This function is further complicated due to fluctuations in the expected number of incident number of photons, electronic "dark noise," and readout error, among others.

pixel number and wavelength, we map the simulated wavelength peak as a function of pixel number. A summary of these is provided in Table 1 above, with rough estimates provided.

Component	Issue	Impacts	Manage By	Predicted Impact	Estimated Error
Lamp Calibration	Absolute Wavelength Accuracy	Wavelength Error	NIST	Small	$\pm 0.002 \text{ \AA}$
	Absolute Radiometric Accuracy	Intensity Error	NIST	Negligible	$\pm ?$ $\text{W/cm}^2/\text{sr}$
Camera	Electron Noise	SNR	Simulation Estimates, Integration Time	Medium	± 25 Electrons
	Photon Noise	SNR	Averaging	Small	Poisson
Simulation	Curve Fitting (Gaussian)	Relative Wavelength Calibration	Improved Fitting Procedures	Negligible	$\pm 10^{-8}$ pixels
	Curve Fitting (Orthogonal Distance Regression)	Relative Wavelength Calibration	Calibration of Diagnostic Lines, Instrument Response Function	Medium	$\pm 0.06 \text{ \AA}$ ($\pm 12 \text{ km/s}$)

Table 1: Summary of known or estimated sources of error and their management strategies.

For our analysis, we must first consider all reasonable sources of error so that we can account for them as we generate the simulation. First, this paper explains how our code generates the simulated signal using a NIST calibrated lamp. We map the incident photon signal onto a detector array by way of a line-spread function. Since the number of photons is a countable source, we have to introduce Poisson error. In addition, converting the signal from number of photons to an electronic readout introduces readout noise.

After the simulated signal at each pixel has been generated with these errors, we perform Gaussian curve-fitting to obtain sub-pixel resolution. Before we use this data to generate the mapping function, we generate the simulated signal multiple times in a Monte-Carlo fashion. This method gives more precision, since we can employ the standard error of the mean from the resulting histograms. Finally, using a polynomial Orthogonal Distance Regression (ODR) method, which takes into account estimated error in

2 Generating and Mapping the Simulated Signal

The diagnostic signal used in this characterization is a Pt/Cr-Ne lamp from Sansonetti et al. [2004]. The lamp produces a signal based on the voltage supplied (see paper sources), see Figure 1.

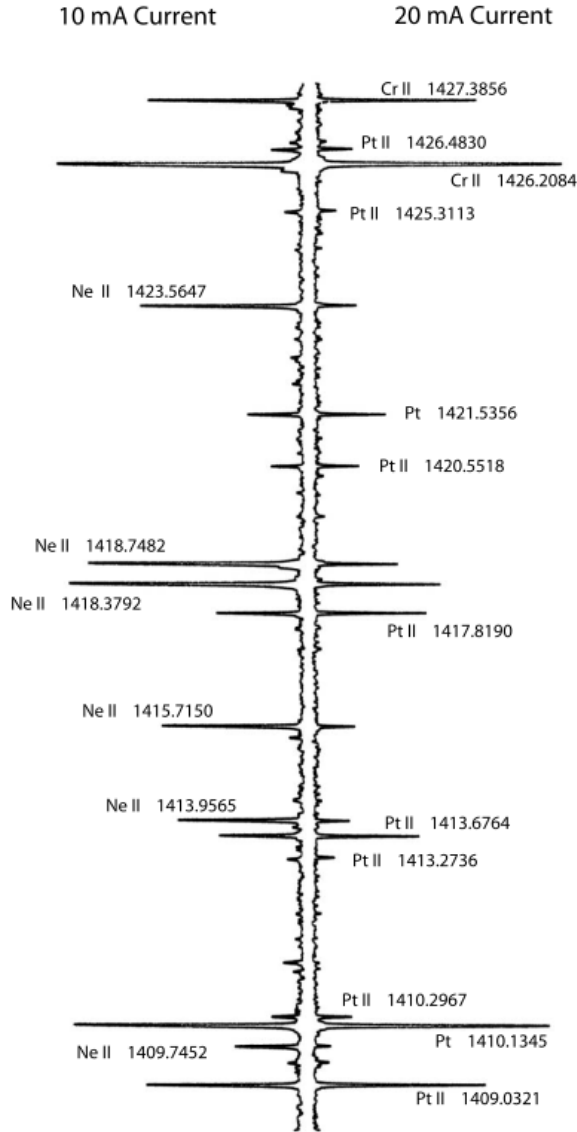


Figure 1: From Sansonetti et al. [2004]: "Tracings of the spectrum of a Pt/Cr-Ne hollow cathode lamp operated at 10 mA (left panel) and 20 mA (right panel) around 1420 Å. Lines of different species are identified with wavelengths given in Å. Note that all Ne II lines are enhanced relative to the Pt II in the 10 mA spectrum".

Treating the file to remove extraneous characters and delimiters, we find that the data only gives the line locations and intensity. Thus, must give the signal a realistic Gaussian width such as

$$I = (I_0 - I_b) e^{-\frac{(\lambda - \lambda_0)^2}{2\sigma^2}} + I_b \quad (1)$$

, where I is the amplitude of the peak intensity I_0 and the background I_b , λ is the wavelength and mean wavelength of the peak λ_0 , and σ is the width. One of

the physical reasons for this spectral spreading is the instrument response function σ_{width} . For now, we set the width through linear interpolation between three measured points.

$$\sigma_{width} = \begin{cases} 0.038 \text{ \AA} & \text{if } \lambda = 1170 \text{ \AA} \\ 0.053 \text{ \AA} & \text{if } \lambda = 1570 \text{ \AA} \\ 0.079 \text{ \AA} & \text{if } \lambda = 1960 \text{ \AA} \end{cases} \quad (2)$$

As this project progresses, we aim to have measured (or simulated) instrument response function data at more discrete intervals. This will allow for a more dynamic simulation. As we will see later on, this line-spreading function will affect the resulting error at higher wavelengths. Additionally, simulating this signal requires us to set up a matrix for the Gaussian to map to. It would be trivial to assign a non-linearity, i.e. by accounting for how the grating itself will spread the signal. However, this is not so important at this stage. Surely there will be many other sources of error in how the signal reaches the detector, but for now we simply want to look at how a signal of any kind is interpreted, and the resulting error in our ability to do so. Thus, we have inherently assigned linearity to the mapping, and we will see how well we can estimate this.

Continuing with the formulae above, we map the signal as transmitted by each cylinder into pixels. This is most easily done by using an array of size equal to that of the CCD array. Therefore, the signal is mapped to discrete points instead of as a continuum. Seen below are those mapped intensities.

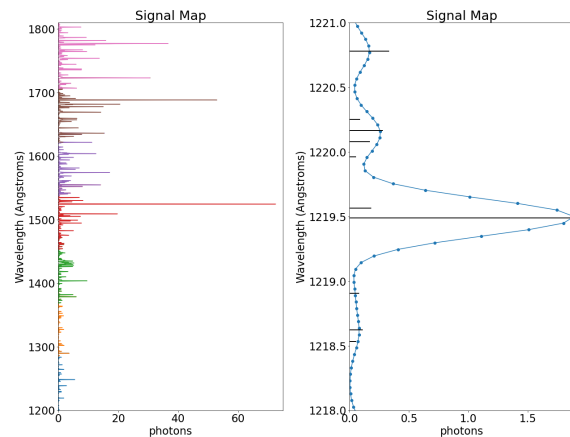


Figure 2: Lamp data in the 1200-1810 Å range relevant to FURST, converted to W/cm² and then to photons. Left: The mapped Gaussian signal received by each of the cylinders. Right: The zoomed figure indicated with markers shows the discrete nature of the pixel array. The horizontal bars provide a representation of where the original signal was located before this mapping and it's rough intensity for scale.

Firstly, note how this Gaussian has been mapped onto discrete pixels. As can be seen in Figure 2 (right), the exact location of each peak will most likely in between pixels. Using this fact, the next section of this paper will discuss the use of a Gaussian fit to obtain sub-pixel precision for these locations. The FURST instrument design achieves the high level of resolution due in part to this multi-cylinder design.

Each cylinder is able to transmit a certain range of wavelengths to the detector. Figure 2 (left) shows how we have designed these ranges such that there is enough overlap to cover the full spectrum range. In reality, these ranges and overlaps may not be equal. For now, this simulation does not distinguish this aspect, but can easily be modified in the future to do so. Secondly, these two plots show the intensity in photons. This conversion process takes into account the effective area, and will be covered in the next section.

3 Converting the Signal to Real Units

To convert the signal intensity to real units, we use the given conversion rate of $2 \cdot 10^{10} W cm^{-2} sr^{-1}$ per arbitrary unit. Multiplying this number by the effective area gives the intensity in W/sr. The effective area is calculated using interpolated values given by the manufacturer of the coatings and mirrors, etc. In practice, we would have higher-resolution data from all of these manufacturers. We have some additional factors including reflection of two mirrors in the collimator, and the fact that the light is smeared into a thin line across the height of the CCD (1024 pixels).

Since each pixel sees about $10 \cdot 10^{-6} sr$, we convert the intensity to be in Watts. We can then divide by the energy per photon (given by $\frac{hc}{\lambda}$) to find the intensity in photons per second. We can also adjust the exposure time and total number of exposures. For now, we use the estimate of 1.1 seconds and 10 exposures in total.

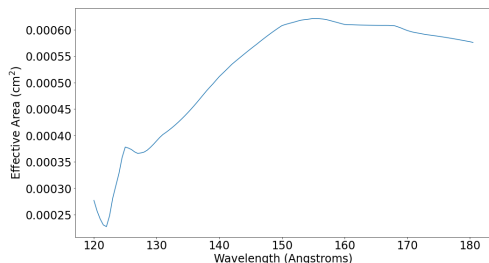


Figure 3: Effective Area of the FURST instrument and Collimator.

This gives the intensity in photons as shown in Figure 2. From here, we add photon noise in an Monte-Carlo-like fashion, which will be discussed later on. Next, using the photon energy $\frac{hc}{\lambda}$ (J/photon) divided by the electron energy $1.602 \cdot 10^{-19}$ (J/electron) we can convert the intensity in photons to electrons. From here, we can add real noise to the electron signal. However, since electronic readout noise and data-number (DN) noise are also part of the Monte-Carlo loop, those will be covered later as well.

4 Monte-Carlo Gaussian-Fitting

As described in the introduction, the mapping function requires knowledge of the expected location of each peak in terms of pixel number. We used a Gaussian function to add line-spreading to each peak. We need to account for random noise in a couple of ways, namely discrete Poisson noise and electronic readout noise.

So far the intensity has been converted to units of photons. Since the CCD is recording a count rate, Poisson noise is added to the signal. Converting to electrons and then to Data Numbers (DNs), we then must add readout noise. This is because the electronic signal transmission is read with a bias of 3000 ± 25 DN. To account for randomness, this is performed in a Monte-Carlo fashion: we add the noise within a loop, and then attempt to recompute the location of the line using a Gaussian curve-fit.

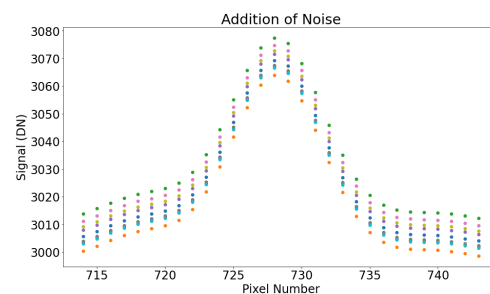


Figure 4: Example of a signal converted to Data Numbers (DNs), with the addition of photon and electronic readout noise.

This curve-fitting function is written in the same form as Equation 1, and is fit using Python's "scipy.optimize.curve_fit" package. In each cylinder's wavelength range, we previously identified the top 5 peaks in each range to use as diagnostic lines. In practice, we will be much more precise about which

lines we use, taking into account other factors such as their spacing throughout the specific range, reliability of the diagnostic lamp, etc. For the simulation here, providing an estimate for these pixel locations, widths, backgrounds, and amplitudes helps the code converge more quickly.

As mentioned already, these sub-pixel-resolution results will be obtained for each exposure. After the addition of noise is repeated several times, the error in this measurement is calculated based on the standard error of the mean as follows.

$$\sigma_M = \sigma/N \quad (3)$$

This gives us a mean location for each peak with the associated error in our knowledge of that peak. Thus, the more exposures N that we take during calibration, the more confident we can be about the location of these peaks. This is vital, since the actual science data may only offer around 10 exposures during flight.

So, the better we can mitigate any such errors associated with calibration, the more we can focus on those other sources. This Monte-Carlo routine is then repeated across the input signals from each cylinder. Now, we have provided simulated data that can be used to directly correlate pixel number to wavelength number. Using a different kind of curve-fitting, the next section will discuss this numerical relation. From here we will only focus on the five most intense source lines from each cylinder range.

5 Fitting Wavelength vs. Pixel

The final stage of this simulation is to find the best-fit the functions for directly correlating pixel number to wavelength. This time, the curve-fitting must take into account the error in both pixel number and wavelength values. To do this we utilize the "scipy.odr" package, which contains an Orthogonal Distance Regression algorithm. For now we have defined the function as a simple 2nd order polynomial of the form

$$\lambda = (\lambda_0 \pm \Delta\lambda_0) + (A \pm \Delta A) \cdot x + (B \pm \Delta B) \cdot x^2 \quad (4)$$

, where x is the pixel value, and the parameters λ , A , and B are listed with their associated error.

Each of these 7 optical signals will have unique mapping functions based on the geometry, reflectivity, etc, and may not be as similar as they are here. In addition, our current mapping is mostly linear. As mentioned before, this assumption was inherently assumed based on the way the signal was simulated.

However, accounting for this possibility now will allow us to account for it later on when the experimental results show otherwise. Below are listed the error results from a single run, with 10 exposures of 5 lines per cylinder range.

Cylinder #	$\Delta\lambda_0$	ΔA	ΔB
1	0.04408	8.76E-05	3.45E-08
2	0.01279	2.88E-05	1.41E-08
3	0.14301	38.8E-05	21.8E-08
4	0.06298	7.87E-05	2.50E-08
5	0.03362	6.87E-05	2.99E-08
6	0.04550	8.87E-05	3.78E-08
7	0.06204	12.7E-05	5.65E-08
Mean	0.05772	12.4E-05	5.95E-08

Table 2: The polynomial correlation at each signal as found by the Orthogonal Distance Regression (ODR) method.

The error in each appears to be quite low, however cylinder #3 seems to have a higher error for the Δ terms. This has been attributed to the reliability of spectral lines within that wavelength range. Thus, special care in choosing diagnostic signals will be taken here in experimental practice. Analysis of these results is better suited in the form of Resolution

$$R = \frac{\lambda}{\Delta\lambda} = \frac{c}{\Delta v} \implies \Delta v = c \frac{\Delta\lambda}{\lambda} \quad (5)$$

, where Δv is the Doppler-shift resolution of the wavelength.

Using the propagation of error, Equation 4 gives us $\Delta\lambda$ as

$$\Delta\lambda = \sqrt{\Delta\lambda_0^2 + (\Delta A \cdot x)^2 + (\Delta B \cdot x^2)^2} \quad (6)$$

, where x is evaluated at pixel number 1 and 2048. If we calculate these values line-by-line, we can find the resolution Δv of each cylinder's range.

Range (Å)	$\Delta\lambda$ (Å)	Δv (km/s)
1200.0 - 1304.0	0.044 - 0.044	11.01 - 10.18
1284.3 - 1388.3	0.013 - 0.013	2.99 - 2.78
1368.7 - 1472.7	0.143 - 0.144	31.32 - 29.33
1453.0 - 1557.0	0.063 - 0.063	12.99 - 12.15
1537.3 - 1641.3	0.034 - 0.034	6.56 - 6.17
1621.7 - 1725.7	0.046 - 0.046	8.41 - 7.94
1706.0 - 1810.0	0.062 - 0.062	10.90 - 10.32
Mean	0.05786	11.65

Table 3: Resolution Δv for each cylinder's range, rounded for simplicity.

To summarize Table 3, the Δv resolution we can obtain will most likely be between 2.8 - 31 km/s, with a mean value around 11.7 km/s. This mean is skewed though, due to one range in particular. As mentioned before, cylinder #3 appears to have only few bright diagnostic lines. In addition, they are not located in an ideal spread across the region. This may explain why it's error is so much higher.

The goal of 3 km/s may still be obtainable, as cylinder #2 shows. Based on many runs of this simulation, the variations seen in this table are understandable and manageable. Given proper diagnostic techniques, we should be able to fit these signals much better. This means that with the given setup and more advanced experimentation, we estimate easily being able to resolve the signal with \approx 12 km/s in spectral resolution, with a possibility of resolving down to 3 km/s given tighter calibration requirements.

6 Results and Conclusions

From a diagnostic lamp signal, adding in the sources of noise and accounting for the line-spread

7 Acknowledgements

Credit should go first and foremost to Dr. Charles Kankelborg and the MSU team for coming up with this unique solution to this much overlooked problem.

Even more thanks go out to my research advisor, Dr. Amy Winebarger, for her many hours of guidance in giving me the opportunity to understand the crazy and exciting world of Sounding Rockets!

Many thanks to my academic advisor Dr. Gary Zank for pointing me in this direction and providing the funding necessary to do so.

Additionally, there are many people within the NASA MSFC Sounding Rocket team and the UAH Space Science Department who deserve gratitude for their help with this work and the many other projects.

As always, I could not do this without the love of God and the continual support from my wife and family.

Thank you!

This material is based upon work supported by the NSF EPSCoR RII-Track-1.2a (Non-invasive plasma diagnostics for LTP) Cooperative Agreement OIA-1655280. Any opinions, findings, and conclusions or recommendations expressed in this material are those of the authors and do not necessarily reflect the views of the National Science Foundation.

function of the instrument, we have developed a mapping function for converting from CCD pixels to Wavelength. Future work may consist of using this relationship in reverse, allowing us to take an input CCD signal, in terms of pixel number and Data Numbers (DNs), and map out the corresponding wavelengths and photon energies.

This simulation is a work in progress, as experimental values will change many of the parameters. Using propagation of error, we have determined that at present case, we will be able to achieve a Doppler-shift resolution of at least 30 km/s, but more likely around 12 km/s.

The goal resolution was set to be 3 km/s. Since the goal is not achieved by this simulation, there is need for improvements in our design and calibration process. One area of follow up research will be in the experimental validation of our camera parameters such as readout noise. Not only will we calibrate with a lab diagnostic signal such as this Pt/Cr-Ne lamp, we are in the progress of developing a program for an on-board radiation "control measurement." This will give us increased accuracy and precision of the gain measurement, and thus improve the readout noise associated with that error.

References

- S Tsuneta, K Ichimoto, Y Katsukawa, S Nagata, M Otsubo, T Shimizu, Y Suematsu, M Nakagiri, M Noguchi, T Tarbell, et al. The solar optical telescope for the hinode mission: an overview. *Solar Physics*, 249(2):167–196, 2008.
- Ryouhei Kano, Takamasa Bando, Noriyuki Narukage, Ryoko Ishikawa, Saku Tsuneta, Yukio Katsukawa, Masahito Kubo, Shin-nosuke Ishikawa, Hirohisa Hara, Toshifumi Shimizu, et al. Chromospheric Lyman-alpha spectro-polarimeter (clasp). In *Space Telescopes and Instrumentation 2012: Ultraviolet to Gamma Ray*, volume 8443, page 84434F. International Society for Optics and Photonics, 2012.
- Shin-nosuke Ishikawa, Masahito Kubo, Yukio Katsukawa, Ryouhei Kano, Noriyuki Narukage, Ryohko Ishikawa, Takamasa Bando, Amy Winebarger, Ken Kobayashi, Javier Trujillo Bueno, et al. Clasp/sj observations of rapid time variations in the Ly α emission in a solar active region. *The Astrophysical Journal*, 846(2):127, 2017.
- Ken Kobayashi, Amy R Winebarger, Sabrina Savage, Patrick Champey, Peter N Cheimets, Edward Hertz, Alexander R Bruccoleri, Jorg Scholvin, Leon

- Golub, Brian Ramsey, et al. The marshall grazing incidence x-ray spectrometer (magixs). In *Space Telescopes and Instrumentation 2018: Ultraviolet to Gamma Ray*, volume 10699, page 1069927. International Society for Optics and Photonics, 2018.
- Ken Kobayashi, Jonathan Cirtain, Amy R Winebarger, Kelly Korreck, Leon Golub, Robert W Walsh, Bart De Pontieu, Craig DeForest, Sergey Kuzin, Sabrina Savage, et al. The high-resolution coronal imager (hi-c). *Solar Physics*, 289(11): 4393–4412, 2014.
- Amy R Winebarger, Bart De Pontieu, Chun Ming Mark Cheung, Juan Martinez-Sykora, Viggo H Hansteen, Paola Testa, Leon Golub, Sabrina L Savage, Jenna Samra, and Katharine Reeves. Unfolding overlappogram data: Preparing for the cool-aid instrument on hi-c flare. *AGUFM*, 2019:SH33A–06, 2019.
- Charles Kankelborg, Philip Judge, Amy Winebarger, Ken Kobayashi, and Roy Smart. Vuv spectroscopy of the sun as a star. In *Solar Physics Department*. Montana State University, 2017.
- TN Woods, FG Eparvier, R Hock, AR Jones, D Woodraska, D Judge, L Didkovsky, J Lean, J Mariska, H Warren, et al. Extreme ultraviolet variability experiment (eve) on the solar dynamics observatory (sdo): Overview of science objectives, instrument design, data products, and model developments. In *The solar dynamics observatory*, pages 115–143. Springer, 2010.
- Craig J Sansonetti, F Kerber, Joseph Reader, and Michael R Rosa. Characterization of the far-ultraviolet spectrum of pt/cr-ne hollow cathode lamps as used on the space telescope imaging spectrograph on board the hubble space telescope. *The Astrophysical Journal Supplement Series*, 153(2): 555, 2004.